Nanoscale Advances

ROYAL SOCIETY OF CHEMISTRY

PAPER

View Article Online
View Journal | View Issue

Open Access Article. Published on 13 October 2021. Downloaded on 2/21/2026 9:12:53 PM.
This article is licensed under a Creative Commons Attribution-NonCommercial 3.0 Unported Licence.

Check for updates

Cite this: *Nanoscale Adv.*, 2022, **4**, 163

Self-assembly of ultra-small-sized carbon nanoparticles in lipid membrane disrupts its integrity

Bing Fang,[a] Xing Dai,[b] Baoyu Li,*[b] Yuanyuan Qu,[a] Yong-Qiang Li,[a] Mingwen Zhao,[a] Yanmei Yang[c] and Weifeng Li*[a]

Received 1st July 2021
Accepted 12th October 2021

DOI: 10.1039/d1na00529d

rsc.li/nanoscale-advances

Although nanomaterials are widely studied in biomedical applications, the major concern of nanotoxicity still exists. Therefore, numerous studies have been conducted on the interactions of various biomolecules with various types of nanomaterials, including carbon nanotubes, graphene, fullerene *etc.* However, the size effect of nanomaterials is poorly documented, especially ultra-small particles. Here, the interactions of the smallest carbon nanoparticle (NP), C_{28}, with the cell membrane were studied using molecular dynamics (MD) simulations. The results show that similar to fullerene C_{60}, the C_{28} NPs can self-assemble into stable clusters in water. Inside the membrane, the C_{28} NPs are more prone to aggregate to form clusters than C_{60} NPs. The reason for C_{28} aggregation is characterized by the potential of mean force (PMF) and can be explained by the polarized nature of C_{28} NPs while the acyl chains of lipids are nonpolar. At the C_{28} cluster regions, the thickness of the membrane is significantly reduced by the C_{28} aggregation. Accordingly, the membrane loses its structural integrity, and translocation of water molecules through it was observed. Thus, these results predict a stronger cytotoxicity to cells than C_{60} NPs. The present findings might shed light on the understanding of the cytotoxicity of NPs with different sizes and would be helpful for the potential biomedical applications of carbon NPs, especially as antibacterial agents.

1. Introduction

With the rapid development of nanotechnology, nanomaterials have attracted enormous attention in various biomedical applications, such as gene detection and gene delivery,[1,2] tumor imaging and therapy,[3–5] biomarkers and probes,[6–8] due to their unique mechanical, optical, and electrical properties.[9–11] Prior to biomedical applications, the major concern of nano-toxicity has attracted extensive attention. Large numbers of theoretical and experimental studies reported the interactions between nanomaterials and biomolecules to understand the mechanistic origins of the bio-toxicity of the nanomaterials. For example, recent studies on the adsorption of proteins onto nanomaterials have shown that both structures and functions of proteins can be severely affected by nanomaterials such as carbon nanotubes and graphene.[12–23] It is reported that carbon nanotubes can either bind to the receptor protein, thus inhibiting the binding of the native ligand, or directly disrupt the active site of the protein.[12–16] In addition, carbon nanotubes can also affect the dynamic properties of proteins, such as binding to the messenger protein CaM, leading to failure in signaling.[17] Recently, the Zhou group reported that defective graphene can denature protein with a higher speed than ideal graphene.[18,19] There are also many studies on the biosafety of fullerenes and their derivatives. For example, C_{60}, the prototype fullerene, is effective in blocking the ion channels of proteins in the membrane.[20] In addition, the Zhao group demonstrated that the metallofullerenol $Gd@C_{82}(OH)_{22}$ can inhibit the functions of WW/SH3 domains by blocking the ligands binding to the active sites.[21–24] These structural and functional changes of biomolecules can lead to cell death.

As the boundary of the cell to the outside environment, the plasma membrane plays an essential role in controlling the cellular substance exchange. Thus, the interactions of the cell membrane with nanomaterials are possibly the primary origins of nano-toxicity, and thus have been studied extensively. For instance, Zhou *et al.* have demonstrated by experimental and theoretical approaches that graphene nanosheets can penetrate into cell membranes and extract phospholipids from them,

[a]School of Physics, Shandong University, Jinan, Shandong, 250100, China. E-mail: lwf@sdu.edu.cn

[b]Institute of Quantitative Biology and Medicine, State Key Laboratory of Radiation Medicine and Protection, School of Radiation Medicine and Protection, Collaborative Innovation Center of Radiation Medicine of Jiangsu Higher Education Institutions, Soochow University, Suzhou 215123, China. E-mail: byli@suda.edu.cn

[c]College of Chemistry, Chemical Engineering and Materials Science, Collaborative Innovation Center of Functionalized Probes for Chemical Imaging in Universities of Shandong, Key Laboratory of Molecular and Nano Probes, Ministry of Education, Institute of Molecular and Nano Science, Shandong Normal University, Jinan, 250014, China

© 2022 The Author(s). Published by the Royal Society of Chemistry

Open Access Article. Published on 13 October 2021. Downloaded on 2/21/2026 9:12:53 PM.
This article is licensed under a Creative Commons Attribution-NonCommercial 3.0 Unported Licence.

causing cell death through disrupting the membrane.[25] Very recently, phosphorene has been shown to have similar molecular mechanisms to destruct cell membranes.[26] Due to the nanoscale size of nanomaterials, their interactions with biomolecules are very sensitive to the shape, size and even elemental components of nanomaterials. Besides the interactions of 2D nanomaterials with cell membranes, NPs with different shapes interacting with cell membranes have also been studied. Fullerene C_{60} is shaped like a football with a small diameter of 0.7 nm which makes it have unique interactions with the cell membrane interior which is also hydrophobic. Because of the hydrophobic nature, C_{60} can easily penetrate into the membrane.[27,28] At high concentrations, C_{60} can form clusters in the membrane and cause deformation of the membrane structure.[28,29] Besides C_{60}, numerous carbon particles have been reported with different diameters. However, the effects of the size of carbon NPs, especially ultra-sized NPs, which match the size of biomolecules (amino acids, nucleotides, phospholipid headgroups), on membranes have not been documented.

In this work, using C_{28}, the experimentally reported smallest NP, as the representative NP, we investigated the binding and distributions of C_{28} NPs in lipid bilayer membranes using molecular dynamics (MD) simulations. Our results reveal that, both in water and membranes, C_{28} NPs can spontaneously assemble into stable clusters. At high concentrations, the C_{28} NPs can aggregate to form clusters inside the membrane. This can cause severe distortion to the membrane structure and cause water translocation through the membrane. This reveals that this ultra-small NP can cause significant strong toxicity which might be even stronger than that of C_{60}. This work helps to better understand the size-effect of NPs on their cytotoxicity and could guide the biomedical application studies of nanostructures.

2. Methods

2.1 Models and simulation setup

The C_{28} NP has a diameter of 0.47 nm, which is the smallest experimentally synthesized endohedral metallofullerene.[30] The C_{28} NP consists of a C_{28} cage and a uranium atom, which is used to stabilize the strongly reactive C_{28} cage.[31–33] With the uranium atom, the C_{28} cage has net atomic charges. This is different from the C_{60} NP which bears no charge and thus is purely hydrophobic.[34] However, while the structures and properties of the C_{28} NP have been well-studied by theoretical and experimental approaches, the interaction process of C_{28} with biomolecules, like lipid membranes, is yet to be reported. The smallest size of the C_{28} particle will bring some diverse results when it interacts with the membrane. Quantum chemical calculations for U@C_{28} were performed using the Gaussian 09 program.[35] The geometry of U@C_{28} was optimized at the PBE/SDD/6-31G* level.[36] The standard Gaussian-type basis sets 6-31G* (ref. 37) were used for C atoms. The Stuttgart/Dresden relativistic effective core potentials (SDD)[38] and their corresponding valence basis sets[39] were applied for the U atom. Single-point energy was calculated for the optimized geometry at the B3LYP/SDD/6-31G* level[40,41] to obtain the ESP of the ground state electron density. Subsequently, the atomic charges fit to the ESP at points selected according to the CHelpG scheme[42] were calculated by using Multiwfn program.[43] These atomic charges were then used for the following classical MD simulations.

The membrane model was constructed using the CHARMM-GUI membrane builder,[44] which is composed of 128 POPC lipids with 64 lipids on each leaflet. The membrane was firstly equilibrated for 10 ns at 300 K and 1 bar pressure, and was used as the initial structure for C_{28} simulation.

Four different systems were used to explore the interactions of different numbers of C_{28} NPs with the membrane: 128 POPC with one C_{28} particle (POPC-1C_{28}), five C_{28} (POPC-5C_{28}), ten C_{28} (POPC-10C_{28}) and twenty C_{28} (POPC-20C_{28}). Initially, the C_{28} NPs were placed with the minimum distance to the lipid membrane surface being larger than 1.0 nm. The complex was then solvated in a water box ($6.5 \times 6.5 \times 10$ nm^3) under periodic boundary conditions. The TIP3P water model was used.[45] The total numbers of atoms are 31 756, 31 749, 31 732 and 31 734 for the four different systems (POPC-1C_{28}, POPC-5C_{28}, POPC-10C_{28}, and POPC-20C_{28}) respectively. In addition to C_{28}-membrane models, control simulations of pure POPC lipids and POPC lipids with twenty C_{60} NPs were also performed for comparison (POPC-20C_{60}). In addition, a simulation of twenty C_{28} NPs in a water box was also performed to investigate the self-assembly behavior of C_{28} NPs.

All the MD simulations were performed with the GROMACS package[46] and the lipids were modeled using the GROMOS53A6 force field.[47] In the simulations, the covalent bonds involving the H atoms were constrained by the LINCS algorithm.[48] The structural configurations were saved every 1 ps for subsequent analysis. The van der Waals (vdW) interactions were calculated with a cutoff distance of 1.0 nm, while the long-range electrostatic interactions were treated with the particle-mesh Ewald (PME) method.[49,50] After energy minimization, the complex systems were equilibrated for 2 ns under the NPT ensemble to achieve 300 K and 1 bar. Then, 2 μs simulation was performed for each system under the NPT ensemble for data collection. The semi-isotropic Berendsen barostat[51] and the v-rescale thermostat[52] were used for pressure coupling and temperature coupling, respectively. Visualizations and analysis were performed using the VMD software package.[53]

2.2 Umbrella sampling MD simulation

The association free energies between two C_{28} NPs in water and POPC membrane are described as the potential of mean force (PMF) using the umbrella sampling technique. The distance between the center of mass (COM) of two C_{28} particles was restrained at certain distance d_0 with a harmonic force

$$F = k \times (d - d_0)$$

where k is the force constant, 3000 kJ mol^{-1} nm^{-2}. The distance d_0 (including x, y and z) was sampled from 0.60 to 1.50 nm with a step of 0.1 nm. At each distance, 10 ns productive simulation has been generated. The final PMF curve was obtained using the weighted histogram analysis method (WHAM).[54]

 © 2022 The Author(s). Published by the Royal Society of Chemistry

Open Access Article. Published on 13 October 2021. Downloaded on 2/21/2026 9:12:53 PM.
This article is licensed under a Creative Commons Attribution-NonCommercial 3.0 Unported Licence.

The PMF of a single C_{28} transferring across the lipid monolayer was also calculated with the umbrella sampling technique. The distance between the COM of C_{28} particle and the COM of the POPC lipids along the normal direction of the membrane was used as a variable. A total of 40 windows were used with a step of 0.1 nm and a force constant of 2000 kJ mol^{-1} nm^{-2}. For each window, 10 ns simulation has been generated.

3. Results and discussion

3.1 The aggregation of C_{28} NPs in water

We firstly simulated the aggregations of twenty C_{28} particles in water as the preliminary case. As shown in Fig. 1(a)–(c), the C_{28} NPs were initially well separated and then quickly aggregated to form clusters in three independent simulations. To quantify the self-assembly behavior of C_{28} NPs, we calculated the number of clusters and monitored the largest cluster size of C_{28} NPs in POPC-20C_{28} as a function of the simulation time. Here, the C_{28} NPs were treated to form a cluster if the minimum distance between the COM of two C_{28} NPs is within 0.98 nm. Here, the value of 0.98 nm corresponds to the first maximum of the PMF for a C_{28} dimer to dissociate in water which is presented later. In addition, an isolated C_{28} particle is treated as the smallest cluster. As shown in Fig. 1(d) and (e), at $t = 0$ ns, the number of clusters and the largest cluster size were respectively 20 and 1 because the NPs were well separated. From 0 ns to 33 ns, the number of clusters gradually reduces and the largest cluster size shows a stepwise increase. After 33 ns, there is no significant change in both the number of clusters and the largest cluster size. At the end of the simulation, the biggest cluster consisting of 12, 9 and 13 C_{28} NPs was formed in three trajectories respectively. This phenomenon is similar to the self-assembly behavior of C_{60} NPs in water because of the generally hydrophobic nature of the two types of NPs. To describe the aggregation behavior of C_{28} NPs in water, we calculated the PMF of two C_{28} NPs as a function of their COM–COM distance. As shown in Fig. 2(c), the minimum at a distance of 0.78 nm corresponds to the direct contact pair (DCP) of two C_{28} NPs. The dissociation energy barrier is about 11 kJ mol^{-1}, thus C_{28} NPs tend to aggregate in water because the DCP state is the global minimum. In addition, we also calculated the PMF of two C_{28} NPs as a function of their COM–COM distance in the membrane. As shown in Fig. 2(c), at a small distance of less than 0.9 nm, the PMF profiles of two C_{28} NPs in water and POPC are almost the same. The reason is that two C_{28} NPs form direct contacts because there is no water or lipid molecules located between them as shown in the 2D density contour maps in Fig. 2(c). Thus the interactions are less affected by the environments. At a larger distance, there are water/lipids between the two C_{28} which can regulate the interacting energy profile, thus the PMF profiles are different at a large distance.

3.2 The intrusion process of C_{28} NPs into the membrane

To better understand the intrusion process of the C_{28} particle into the membrane, we firstly simulated one C_{28} particle interacting with the membrane. The location of C_{28} (measured from COM) with respect to the membrane is calculated to reflect the C_{28} position and shown in Fig. 3(a). At the beginning of the simulation, the C_{28} particle and membrane were well separated, and the C_{28} particle stayed in the bulk water with a distance 3.0 nm away from the center of the membrane. Then the C_{28} particle quickly loaded to the surface of membrane at about $t =$ 50 ns, and the COM distance quickly decreases to ~2.0 nm.

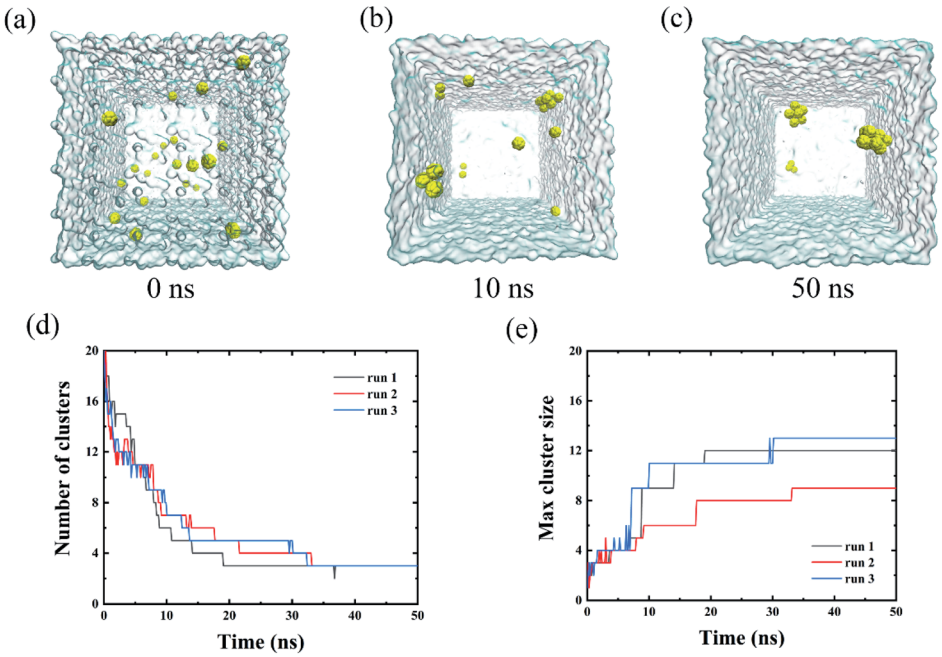

Fig. 1 (a)–(c) Three representative structures at different simulated time points of 20 NPs in water. (d) The number of aggregated clusters and (e) the largest cluster size as a function of simulation time.

Open Access Article. Published on 13 October 2021. Downloaded on 2/21/2026 9:12:53 PM.
This article is licensed under a Creative Commons Attribution-NonCommercial 3.0 Unported Licence.

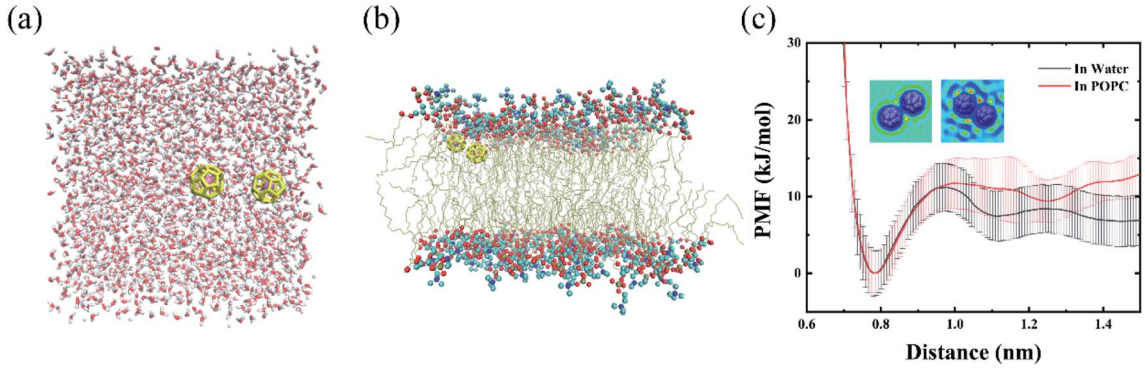

Fig. 2 Snapshots of two C_{28} NPs in water (a) and membrane (b) used in umbrella sampling simulations. For clarity, the water molecules are not shown in (b). (c) The free energy profiles of two C_{28} NPs with respect to their COM–COM distance in water and POPC membrane. The direct contacting state (DCS) at 0.78 nm is considered to have a free energy of zero. In (c), the two dimensional density contour maps of the water (left) and lipids (right) of C_{28} in a cross-section at the COM–COM distance of 0.90 nm are shown.

Then, the curve declines sharply because the C_{28} particle intruded into the membrane. We noticed that the C_{28} prefers to stay at the position which is ~1.0 nm away from the center of the membrane although random translocations between the two leaflets of the membrane were detected. In detail, three translocation cases happened in 2000 ns simulation. This tendency has also been observed in previous atomistic simulations where C_{60} particles stayed 1.0 nm away from the membrane center. The dotted line in the middle in Fig. 3(a) is the center of the membrane. In Fig. 3(b), the location of the density peaks of the PCN (the phosphate and part of the choline) can be regarded as the upper and lower boundaries of the membrane which are represented by the two dotted lines in Fig. 3(a).

To better characterize the binding affinity between the C_{28} and the membrane, we calculated the PMF of the C_{28} particle during insertion into the membrane. As shown in Fig. 3(c), the PMF is a two-step decrease from bulk water to the membrane interior. The first step is from the water to the membrane boundary (from 4 nm to 2.25 nm) where the energy well is about -14.84 kJ mol^{-1}. Then the C_{28} particle overcomes the energy barrier of approximately 2 kJ mol^{-1} to pass through the membrane surface. This phenomenon has been reported for various types of nanoparticles interacting with the membrane. For instance, the Gao Huajian group reported that the energy profiles of NPs with various types of shapes uniformly show a barrier at the water–bilayer interface.[55,56] This is due to the fact that the head groups of lipids are highly charged resulting in high density and high viscosity. The second step is from the inner side of the hydrophobic region to the position 1 nm away from the center of the membrane with an energy decrease of -17.54 kJ mol^{-1}. When the C_{28} particle further moves to the membrane center (from 1.02 nm to 0 nm), it will be hindered by a ~9 kJ mol^{-1} energy barrier. Therefore, the C_{28} particle prefers to locate at the position which is 1.0 nm away from the center of the membrane. To understand the origin of this PMF barrier, Marrink *et al.* simulated the insertion of C_{60} into the membrane and found that the stable position of C_{60} is about 0.7 to 1.3 nm

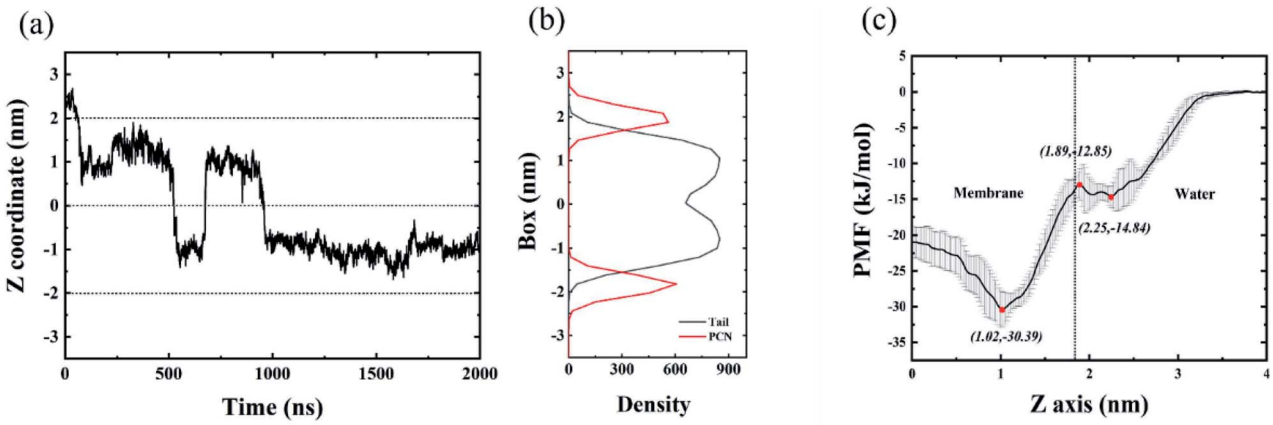

Fig. 3 (a) The z coordinate of the C_{28} particle in the membrane as a function of the simulation time, the three dashed lines indicate the borderlines of the membrane to water and the center of the membrane which is shown in (b). Density profiles for PCN (the phosphate and part of the choline (CH_2CH_2N)) and the fatty acid tails of the lipid as a function of the distance from the membrane center ($z = 0$). (c) PMF of a C_{28} particle from water into the center of the bilayer ($z = 0$). Error bar is also shown.

 © 2022 The Author(s). Published by the Royal Society of Chemistry

Open Access Article. Published on 13 October 2021. Downloaded on 2/21/2026 9:12:53 PM.
This article is licensed under a Creative Commons Attribution-NonCommercial 3.0 Unported Licence.

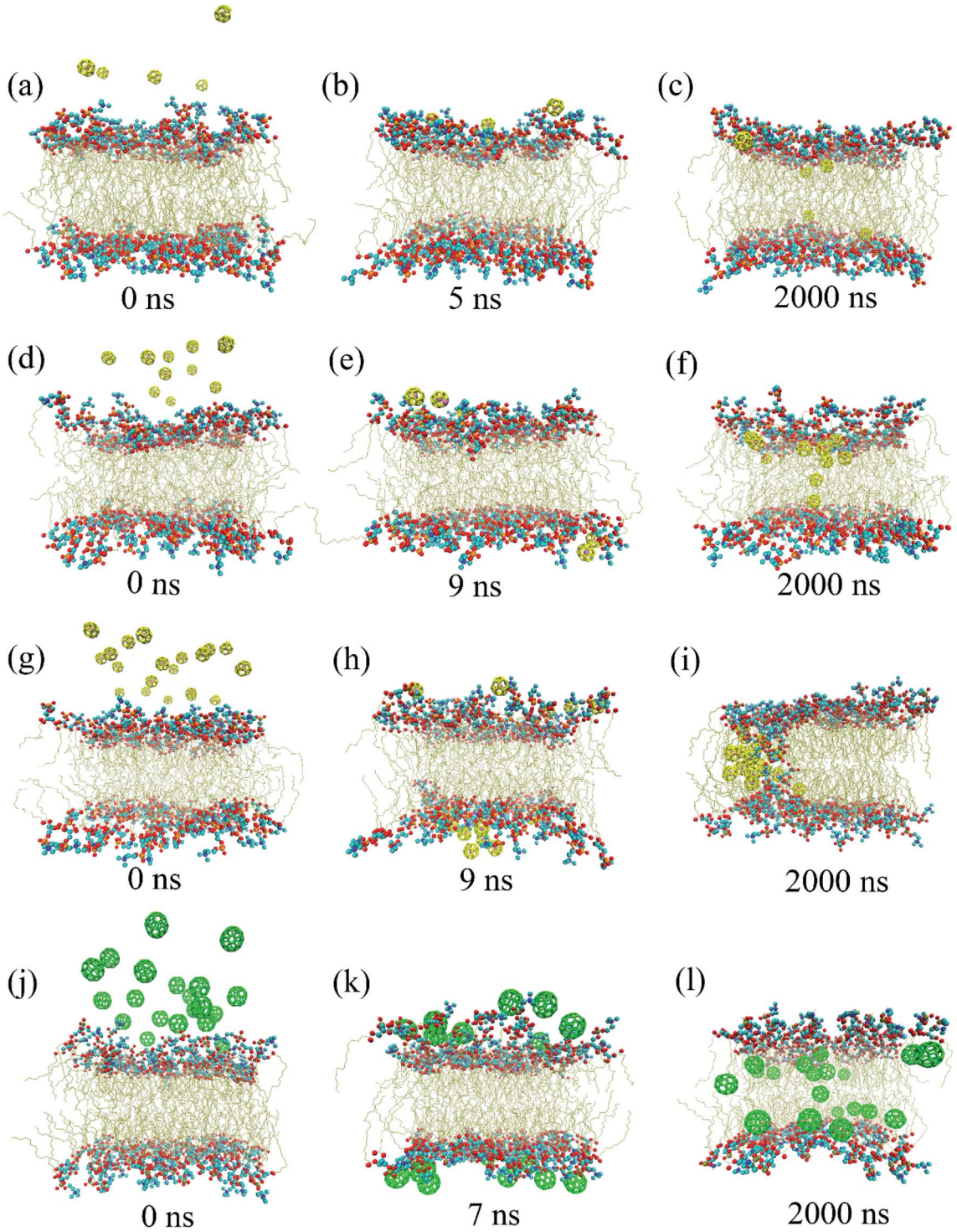

Fig. 4 Three representative structures at different simulation times in the POPC-5C_{28} (a)–(c), POPC-10C_{28} (d)–(f), POPC-20C_{28} (g)–(i) and POPC-10C_{60} (j)–(l) systems. Oxygen (red), nitrogen (blue), carbon (cyan), and phosphorus (orange) atoms in head groups are shown as spheres, while the phospholipids are represented as a tan line. The C_{28} and C_{60} NPs are shown in yellow and green color respectively. For clarity, the water molecules are not shown.

away from the center of the membrane.[57] This is similar to our present study of C_{28} although the specific position differs. They proposed that the friction coefficient increases upon increasing the penetrant size, making it difficult for the penetrant to pass through this region. This is well consistent with unbiased MD results in Fig. 3(a).

In order to investigate whether a similar phenomenon occurs when a large number of C_{28} intrudes into the membrane,

Open Access Article. Published on 13 October 2021. Downloaded on 2/21/2026 9:12:53 PM.
This article is licensed under a Creative Commons Attribution-NonCommercial 3.0 Unported Licence.

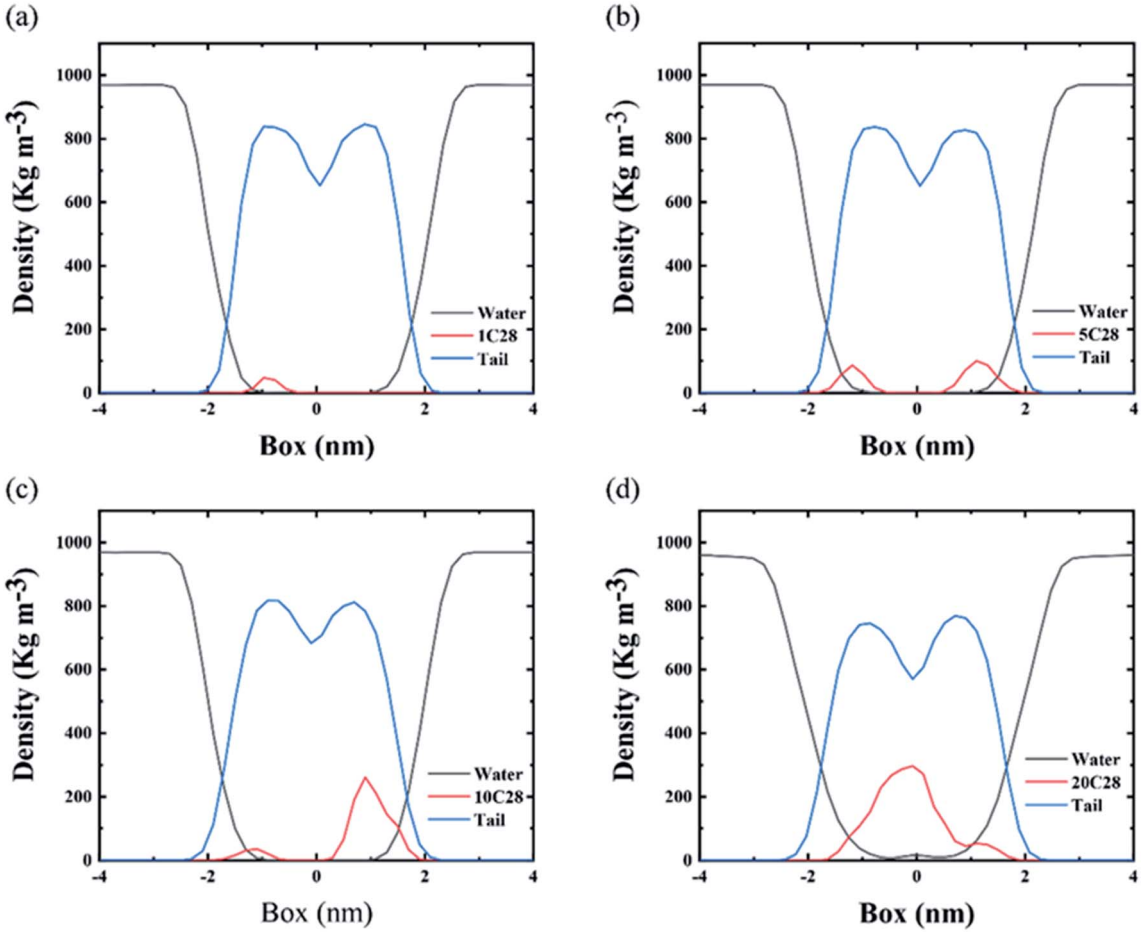

Fig. 5 Density profiles for various parts as a function of the distance from the membrane center ($z = 0$) in the POPC-1C_{28} (a), POPC-5C_{28} (b), POPC-10C_{28} (c) and POPC-20C_{28} (d) systems. All the data are averaged over the last 200 ns simulation.

up to 2000 ns simulations were generated for the three systems (POPC-5C_{28}, POPC-10C_{28}, POPC-20C_{28}). Fig. 4 summarizes three representative structures during 2000 ns simulations for the POPC-5C_{28} (Fig. 4(a)–(c)), POPC-10C_{28} (Fig. 4(d)–(f)) and POPC-20C_{28} (Fig. 4(g)–(i)). At $t = 0$ ns, the C_{28} NPs uniformly stayed in the bulk water and away from the membrane. Then the C_{28} NPs quickly loaded the surface of the lipid membrane within a few nanoseconds. Thereafter, the C_{28} NPs began to intrude into the lipid membrane. Once they penetrated into the membrane interior, the C_{28} NPs stayed in the membrane and outward translocation back to the bulk water was never observed.

The three systems reveal different distributions of C_{28} in the membrane. For a small C_{28} ratio of POPC-5C_{28} and POPC-10C_{28}, C_{28} NPs are generally dispersed in the membrane. In contrast, at a high C_{28} ratio, the distribution of C_{28} in the membrane is different. As shown in Fig. 4(g)–(i), the C_{28} NPs aggregated and formed a large cluster after penetrating into the membrane interior. This phenomenon is different from the two simulations with low C_{28} concentration in Fig. 4(a)–(f), which is also in sharp contrast to the C_{60} NPs in the membrane, where the aggregation degree of C_{60} NPs was significantly lower (Fig. 4(l)). The aggregation behavior of C_{28} can be explained by the polarized nature of C_{28} NPs while the acyl chains of lipids are nonpolar. Thus, inside the membrane, C_{60} NPs (totally nonpolar) are better dispersed than C_{28} (partially polar). More importantly, the C_{28} cluster caused severe structure disruption to the membrane as shown in Fig. 4(i) where the polar "heads" of lipids were found in the interior of the membrane.

In order to describe the distributions of different number of C_{28} NPs inside the membrane, we calculated the density profiles of various components of the model including water, C_{28} and lipid tail across the bilayer normal direction. Here, the density profiles were calculated from the last 200 ns of each simulation. As shown in Fig. 5(a)–(c), at low C_{28} ratio, POPC-1C_{28}, POPC-5C_{28} and POPC-10C_{28}, the density peaks of C_{28} are mainly distributed at the position which is about 1.0 nm away from the membrane center while at the center of the membrane the existence of C_{28} is rare. In contrast, for the POPC-20C_{28} system, a clear peak of C_{28} appears at the center of the membrane, indicating strong aggregation of 20C_{28} inside the membrane.

To quantitatively assess the tendency of C_{28} aggregation in the membrane, we compared the PMF of two C_{28} NPs as a function of their COM–COM distance in water and the membrane. As shown in Fig. 2(c), the dissociation energy barrier in the membrane is about 12 kJ mol^{-1}. At a distance of 1.5 nm (fully separated state), the free-energy in POPC is

 © 2022 The Author(s). Published by the Royal Society of Chemistry

Open Access Article. Published on 13 October 2021. Downloaded on 2/21/2026 9:12:53 PM.
This article is licensed under a Creative Commons Attribution-NonCommercial 3.0 Unported Licence.

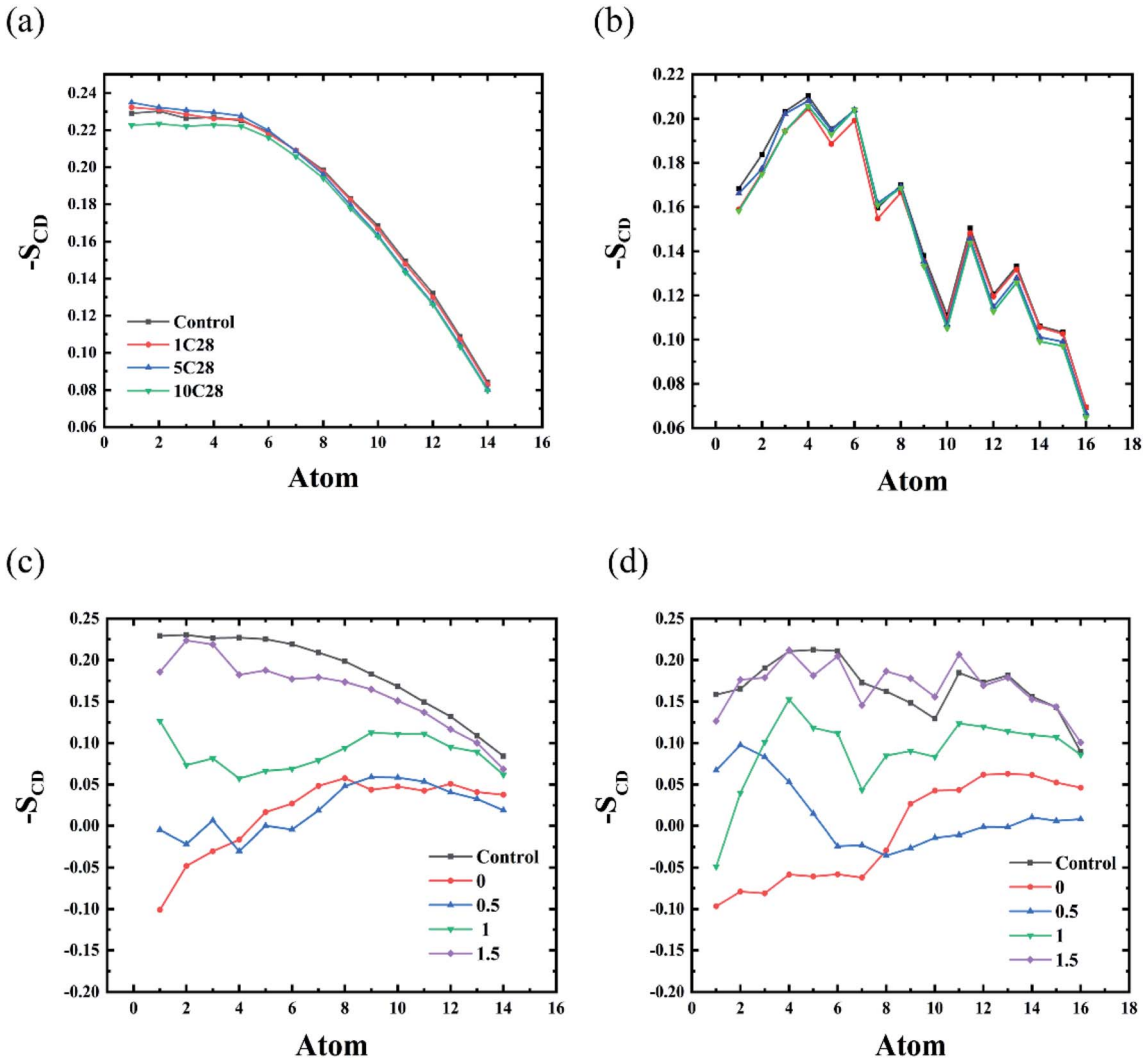

Fig. 6 The deuterium order parameters S_{CD} of the whole membrane calculated for the sn-1 (a) and sn-2 (b) fatty acyl chains for the pure membrane, POPC-1C_{28}, POPC-5C_{28} and POPC-10C_{28} systems. For POPC-20C_{28}, the deuterium order parameters S_{CD} of lipids at different distances from the cluster were calculated for the sn-1 (c) and sn-2 (d) fatty acyl chains.

approximately 13 kJ mol^{-1}, which is larger than 6.8 kJ mol^{-1} in water. The results indicate that C_{28} NPs have a biased tendency to aggregate into a large cluster in the membrane and the cluster is very stable. After overcoming the dissociation energy barrier, the PMF curve is relatively smooth, indicating that the aggregations of C_{28} occur only at high concentrations.

3.3 The effect of C_{28} and C_{60} NPs on POPC membrane structure integrity

Many nanomaterials, such as C_{60}, graphene, phosphorene, and phosphorene carbide, can damage the structural integrity of membranes.[25–27,58] The C_{28} NPs also can lead to the deformation of the membrane, because of the aggregation of C_{28} in the lipid bilayer. In order to investigate the effect of C_{28} on the lipid membrane, we firstly calculated the deuterium order parameters S_{CD} of lipid bilayers in the four simulated systems. It is generally known that S_{CD} can well describe the average orientation of the deuterium bond vector with respect to the bilayer normal direction. Here, the S_{CD} parameters for two carbon chains, sn-1 and sn-2, were calculated according to the following equation[59]

$$S_{CD} = \frac{3\langle\cos^2\theta\rangle - 1}{2}$$

where θ is the angle between the bilayer normal and the vector from C_i to its deuterium atom, and angular brackets represent an ensemble average.

The deformation induced by C_{28} NPs on the membrane depends on its concentration. At low concentrations of C_{28} (POPC-1C_{28}, POPC-5C_{28}, POPC-10C_{28}), C_{28} NPs are dispersed in the membrane, so we calculated the deuterium order parameter for the whole membrane over the last 200 ns of each simulation. As shown in Fig. 6(a) and (b), compared to the pure membrane, only slight changes of S_{CD} curves were observed upon the C_{28} insertion in the POPC-1C_{28}, POPC-5C_{28} and POPC-10C_{28} systems. Thus, at low concentrations, C_{28} NPs caused negligible

Open Access Article. Published on 13 October 2021. Downloaded on 2/21/2026 9:12:53 PM.
This article is licensed under a Creative Commons Attribution-NonCommercial 3.0 Unported Licence.

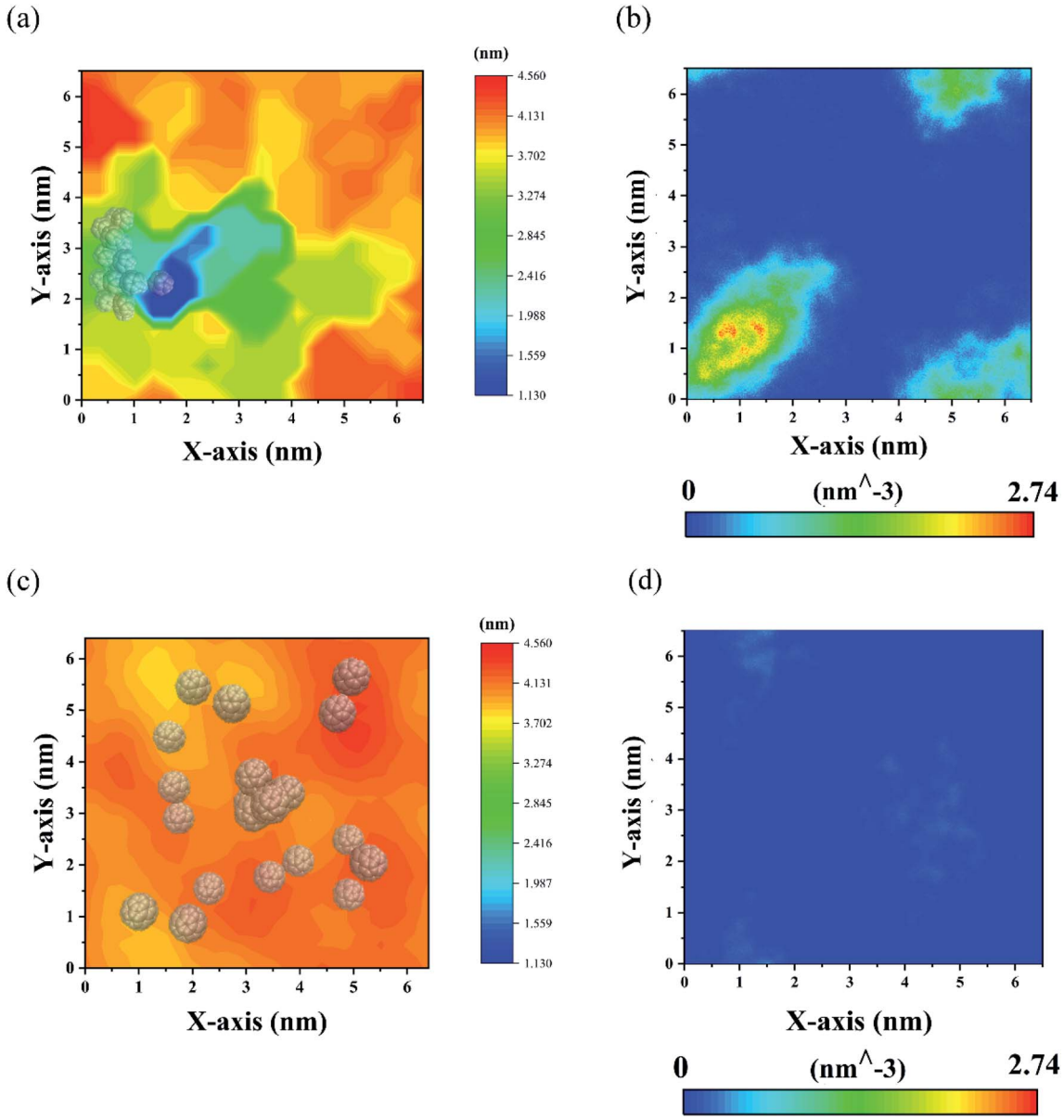

Fig. 7 2D thickness contour of the membrane of (a) POPC-20C_{28} and (c) POPC-20C_{60}, (b) and (d) depict the relative water density in the membrane. The locations of the C_{28} and C_{60} NPs are also shown in (a) and (c).

changes to the membrane. This is because of both the ultra-size of C_{28} and the disaggregation inside the membrane. In contrast, for the POPC-20C_{28} system, the C_{28} NPs aggregated into a large cluster, so we calculated the S_{CD} of lipids with respect to distances of lipids from the C_{28} cluster. As shown in Fig. 6(c) and (d), when the lipids are close to the C_{28} clusters, there was a significant change in S_{CD}, indicating significant distortion of the membrane. However, the effect of the C_{28} cluster on lipids gradually decreases with the increase of distance. At a distance of 1.5 nm, the S_{CD} curve is very close to the normal value. This indicates that the effect of C_{28} NPs on the membrane structure is local.

The change of membrane structure of POPC-20C_{28} can be directly assessed by the membrane thickness which was calculated by the software GridMAT-MD.[60] As shown in Fig. 7(a), the thickness of the membrane is significantly decreased near the C_{28} cluster, which is due to the large number of C_{28} NPs invading the membrane and attracting the head groups of lipids toward the center of the membrane. As shown in Fig. 7(b), this usually results in translocations of water through the membrane which can cause cell death during the experiment.[25] However, distant from the C_{28} cluster, the thickness of the membrane gradually recovered to the normal value (3.85 nm). This is in line with S_{CD} results in Fig. 6(c) and (d) that the C_{28} cluster has a significant but localized effect on the lipid structure. In contrast, for twenty C_{60} in the membrane, the change of membrane thickness is much less than that of C_{28} NPs with the same concentration as can be seen in Fig. 7(c). Moreover, there

 © 2022 The Author(s). Published by the Royal Society of Chemistry

Open Access Article. Published on 13 October 2021. Downloaded on 2/21/2026 9:12:53 PM.
This article is licensed under a Creative Commons Attribution-NonCommercial 3.0 Unported Licence.

are almost no water molecules in the membrane which is in sharp contrast to the case of C_{28}. Thus, at high concentrations, the C_{28} NPs have a larger effect on the structural integrity of membrane lipids than C_{60} NPs. This might point to a stronger cytotoxicity for the cell which surely deserves further experimental validation.

4. Conclusion

In summary, we investigated the interactions of the sub-nanometer C_{28} particles in a lipid membrane using molecular dynamics (MD) simulations. The results show that similar to C_{60}, the C_{28} NPs can self-assemble into stable clusters in water. In the membrane, the C_{28} NPs are more prone to aggregate into big clusters than C_{60} NPs. Thus, C_{28} clusters have a larger effect on the structural integrity of membrane lipids than C_{60} NPs and the thickness of the membrane is significantly reduced by the C_{28} clusters, causing water translocation. The reason for this phenomenon is characterized by the potential of mean force (PMF) and can be explained by the polarization nature of C_{28} NPs while the acyl chains of lipids are nonpolar. By comparing the structural changes of the membrane with the existence of C_{28} or C_{60}, a possibly stronger cytotoxicity of C_{28} is proposed which deserves future experimental validation. This finding is of crucial importance in terms of the biosafety of ultra-small carbon NPs.

Conflicts of interest

There are no conficts to declare.

Acknowledgements

This work is supported by the Natural Science Foundation of Shandong Province (ZR2020MB074, ZR2020JQ04), and National Natural Science Foundation of China (11874238).

References

1 H. Bao, Y. Pan, Y. Ping, N. G. Sahoo, T. Wu, L. Li, J. Li and L. H. Gan, *Small*, 2011, **7**, 1569–1578.
2 Y. Wang, X. Bai, W. Wen, X. Zhang and S. Wang, *ACS Appl. Mater. Interfaces*, 2015, **7**, 18872–18879.
3 H. Sharma and S. Mondal, *Int. J. Mol. Sci.*, 2020, **21**, 6280.
4 Z. Liu, S. Li, X. Xia, Z. Zhu, L. Chen and Z. Chen, *Small Methods*, 2020, **4**, 1900440.
5 Y. Cheng, R. A. Morshed, B. Auffinger, A. L. Tobias and M. S. Lesniak, *Adv. Drug Delivery Rev.*, 2014, **66**, 42–57.
6 H. Asadi and R. P. Ramasamy, *J. Electrochem. Soc.*, 2020, **167**, 167523.
7 A. B. Chinen, C. M. Guan, J. R. Ferrer, S. N. Barnaby, T. J. Merkel and C. A. Mirkin, *Chem. Rev.*, 2015, **115**, 10530–10574.
8 F. Gong, L. Cheng and Z. Liu, *Laser and Optoelectronics Progress*, 2020, **57**, 35–54.
9 L. Z. Feng and Z. A. Liu, *Nanomedicine*, 2011, **6**, 317–324.
10 V. C. Sanchez, A. Jachak, R. H. Hurt and A. B. Kane, *Chem. Res. Toxicol.*, 2012, **25**, 15–34.
11 A. K. Geim, *Science*, 2009, **324**, 1530–1534.
12 V. E. Kagan, N. V. Konduru, W. Feng, B. L. Allen, J. Conroy, Y. Volkov, I. I. Vlasova, N. A. Belikova, N. Yanamala, A. Kapralov, Y. Y. Tyurina, J. Shi, E. R. Kisin, A. R. Murray, J. Franks, D. Stolz, P. Gou, J. Klein-Seetharaman, B. Fadeel, A. Star and A. A. Shvedova, *Nat. Nanotechnol.*, 2010, **5**, 354–359.
13 X. Zhao and R. Liu, *Environ. Int.*, 2012, **40**, 244–255.
14 G. Zuo, Q. Huang, G. Wei, R. Zhou and H. Fang, *ACS Nano*, 2010, **4**, 7508–7514.
15 G. Zuo, X. Zhou, Q. Huang, H. Fang and R. Zhou, *J. Phys. Chem. C*, 2011, **115**, 23323–23328.
16 G. Zuo, S. G. Kang, P. Xiu, Y. Zhao and R. Zhou, *Small*, 2013, **9**, 1546–1556.
17 J. Gao, L. Wang, S. G. Kang, L. Zhao, M. Ji, C. Chen, Y. Zhao, R. Zhou and J. Li, *Nanoscale*, 2014, **6**, 12828–12837.
18 B. Li, D. R. Bell, Z. Gu, W. Li and R. Zhou, *Carbon*, 2019, **146**, 257–264.
19 Z. Gu, W. Song, S. H. Chen, B. Li, W. Li and R. Zhou, *Nanoscale*, 2019, **11**, 19362–19369.
20 M. Calvaresi, S. Furini, C. Domene, A. Bottoni and F. Zerbetto, *ACS Nano*, 2015, **9**, 4827–4834.
21 S. Kraszewski, M. Tarek, W. Treptow and C. Ramseyer, *ACS Nano*, 2010, **4**, 4158–4164.
22 M. Calvaresi, S. Furini, C. Domene, A. Bottoni and F. Zerbetto, *ACS Nano*, 2015, **9**, 4827–4834.
23 S. G. Kang, T. Huynh and R. Zhou, *Nanoscale*, 2013, **5**, 2703–2712.
24 S. G. Kang, T. Huynh and R. Zhou, *Sci. Rep.*, 2012, **2**, 957.
25 Y. Tu, M. Lv, P. Xiu, T. Huynh, M. Zhang, M. Castelli, Z. Liu, Q. Huang, C. Fan, H. Fang and R. Zhou, *Nat. Nanotechnol.*, 2013, **8**, 594–601.
26 W. Zhang, Y. Chen, T. Huynh, Y. Yang, X. Yang and R. Zhou, *Nanoscale*, 2020, **12**, 2810–2819.
27 S. Zhang, Y. Mu, J. Zhang and W. Xu, *PLoS One*, 2013, **8**, e77436.
28 K. A. Russ, P. Elvati, T. L. Parsonage, A. Dews, J. A. Jarvis, M. Ray, B. Schneider, P. J. Smith, P. T. Williamson, A. Violi and M. A. Philbert, *Nanoscale*, 2016, **8**, 4134–4144.
29 M. E. Bozdaganyan, P. S. Orekhov, A. K. Shaytan and K. V. Shaitan, *PLoS One*, 2014, **9**, e102487.
30 P. W. Dunk, N. K. Kaiser, M. Mulet-Gas, A. Rodriguez-Fortea, J. M. Poblet, H. Shinohara, C. L. Hendrickson, A. G. Marshall and H. W. Kroto, *J. Am. Chem. Soc.*, 2012, **134**, 9380–9389.
31 D. Xu, W. Xie, Y. Gao, W. Jiang and Z. Wang, *Chem. Phys. Lett.*, 2018, **712**, 20–24.
32 A. Miralrio and L. E. Sansores, *Comput. Theor. Chem.*, 2016, **1083**, 53–63.
33 A. Munoz-Castro and R. Bruce King, *J. Comput. Chem.*, 2017, **38**, 44–50.
34 Y. N. Makurin, A. A. Sofronov, A. I. Gusev and A. L. Ivanovsky, *Chem. Phys.*, 2001, **270**, 293–308.
35 M. Frisch, G. Trucks, H. Schlegel, G. Scuseria, M. Robb, J. Cheeseman, G. Scalmani, V. Barone, B. Mennucci and G. Petersson, *Gaussian 09*, 2009.

Open Access Article. Published on 13 October 2021. Downloaded on 2/21/2026 9:12:53 PM.
This article is licensed under a Creative Commons Attribution-NonCommercial 3.0 Unported Licence.

36 J. P. Perdew, K. Burke and M. Ernzerhof, *Phys. Rev. Lett.*, 1996, **77**, 3865.
37 W. Hehre, R. Ditchfield and J. Pople, *J. Chem. Phys.*, 1972, **56**, 2257.
38 W. Küchle, M. Dolg, H. Stoll and H. Preuss, *J. Chem. Phys.*, 1994, **100**, 7535–7542.
39 X. Cao and M. Dolg, *J. Mol. Struct.: THEOCHEM*, 2004, **673**, 203–209.
40 A. D. Becke, *J. Chem. Phys.*, 1993, **98**, 5648–5652.
41 C. Lee, W. Yang and R. G. Parr, *Phys. Rev. B: Condens. Matter Mater. Phys.*, 1988, **37**, 785.
42 C. M. Breneman and K. B. Wiberg, *J. Comput. Chem.*, 1990, **11**, 361–373.
43 T. Lu and F. Chen, *J. Comput. Chem.*, 2012, **33**, 580–592.
44 B. R. Brooks, R. E. Bruccoleri, B. D. Olafson, D. J. States, S. Swaminathan and M. Karplus, *J. Comput. Chem.*, 1982, **4**, 187–217.
45 W. L. Jorgensen, J. Chandrasekhar, J. D. Madura, R. W. Impey and M. L. Klein, *J. Chem. Phys.*, 1983, **79**, 926–935.
46 M. J. Abraham, T. Murtola, R. Schulz, S. Páll, J. C. Smith, B. Hess and E. Lindahl, *SoftwareX*, 2015, **1–2**, 19–25.
47 C. Oostenbrink, A. Villa, A. E. Mark and W. F. van Gunsteren, *J. Comput. Chem.*, 2004, **25**, 1656–1676.
48 B. Hess, H. Bekker, H. J. C. Berendsen and J. G. E. M. Fraaije, *J. Comput. Chem.*, 1997, **18**, 1463–1472.
49 T. Darden, D. York and L. Pedersen, *J. Chem. Phys.*, 1993, **98**, 10089–10092.
50 U. Essmann, L. Perera, M. L. Berkowitz, T. Darden, H. Lee and L. G. Pedersen, *J. Chem. Phys.*, 1995, **103**, 8577–8593.
51 H. J. C. Berendsen, J. P. M. Postma, W. F. van Gunsteren, A. DiNola and J. R. Haak, *J. Chem. Phys.*, 1984, **81**, 3684–3690.
52 G. Bussi, D. Donadio and M. Parrinello, *J. Chem. Phys.*, 2007, **126**, 014101.
53 W. Humphrey, A. Dalke and K. Schulten, *J. Mol. Graphics*, 1996, **14**, 33–38.
54 S. Kumar, J. M. Rosenberg, D. Bouzida, R. H. Swendsen and P. A. Kollman, *J. Comput. Chem.*, 1992, **13**, 1011–1021.
55 Y. Li, H. Yuan, A. von dem Bussche, M. Creighton, R. H. Hurt, A. B. Kane and H. Gao, *Proc. Natl. Acad. Sci. U. S. A.*, 2013, **110**, 12295–12300.
56 C. Shen, G. Zou, W. Guo and H. Gao, *Carbon*, 2020, **164**, 391–397.
57 S. J. Marrink and H. J. C. Berendsen, *J. Phys. Chem.*, 1996, **100**, 16729–16738.
58 Y. Liu, Y. Yang, Y. Qu, Y. Q. Li, M. Zhao and W. Li, *Phys. Chem. Chem. Phys.*, 2020, **22**, 23268–23275.
59 D. P. Tieleman, S. J. Marrink and H. J. C. Berendsen, *Biochim. Biophys. Acta, Rev. Biomembr.*, 1997, **1331**, 235–270.
60 W. J. Allen, J. A. Lemkul and D. R. Bevan, *J. Comput. Chem.*, 2009, **30**, 1952–1958.

 © 2022 The Author(s). Published by the Royal Society of Chemistry